Acta Astronautica 207 (2023) 340–352

Contents lists available at ScienceDirect

Acta Astronautica

journal homepage: www.elsevier.com/locate/actaastro

Research paper

Guidance for autonomous spacecraft repointing under attitude constraints and actuator limitations☆

Alison Ponche [a,*], Andrés Marcos [a], Thomas Ott [b], Ramin Geshnizjani [b], Johannes Loehr [b]

[a] University Carlos III de Madrid, Av. de la Universidad 30, 28911, Leganes, Spain
[b] Airbus Defence and Space GmbH, Claude-Dornier-Straße, 88090, Immenstaad, Germany

ARTICLE INFO

Keywords:
Constrained guidance
Online computation
Momentum envelopes

ABSTRACT

Current and future space observation missions need to perform many large-angle, multi-axis slew maneuvers between observations while keeping the scientific instrument's attitude in a safe region. The state-of-practice typically divides each multi-axis maneuver into a series of single-axis sub-maneuvers, each of which is computed by restricting its guidance solution to the exact spacecraft momentum capacity. This ensures that the constraints are explicitly considered and results in a simple on-board implementation of the guidance algorithm, but is time-consuming and non-optimal for the whole multi-axis maneuver. Addressing this issue, this article presents a novel analytical guidance approach that relies on the convexity of the permissible attitude zone. The proposed guidance is time-optimal for a given spacecraft design and set of admissible observation targets. Both guidance approaches are compared using a multi-body/multi-actuator benchmark spacecraft, whose complex repointing phase requires an autonomous on-board guidance computation. It is shown that the proposed approach is systematic and that the reduction in maneuver time, compared to the state-of-practice approach, is considerable.

1. Introduction

Observation spacecraft need to perform many (i.e., more than 1500 per year) large angle and precise attitude slew maneuvers between the observations while satisfying safety critical attitude constraints. These attitude constraints are due to the thermal high sensitivity of the scientific instruments. For instance, space telescopes must prevent sunlight from entering their field of view [1–5], while sun observation spacecraft shall maintain heat shields accurately pointing at the Sun throughout all scenarios [6,7]. These attitude exclusion zones are hard constraints and their violation could lead to the loss of the mission.

Moreover, these missions aim to improve the scientific return by maximizing the image quality and resolution. This is achieved by augmenting the telescope's objective aperture, and thus its focal length. This leads to designing massive space observatories. To further improve the scientific performance, new space observation missions rely on the use of multi-body and multi-actuator (MB/MA) spacecraft architectures. They enable to observe the same target successively with different on-board instruments by using a common movable focusing device. But the trade-off from this higher scientific return is that these types of MB/MA space systems represent a challenge for attitude control design. Indeed, the repointing of such spacecraft involves both a focusing device steering towards the line of sight (LoS) of the observing instrument and a spacecraft slew maneuver. The MB/MA effects induced by these motions and the non-collocated attitude sensors require new attitude guidance and control architectures.

There are two main types of scientific observations: planned and unplanned. For the former, it is important to maximize the time availability during the mission life-time. The latter arise when spontaneous and time-finite events occur and it is scientifically advantageous to observe them. These observations may require to slew the spacecraft

☆ The results presented in this article are the outcome of the Ph.D. project MACON "Integrated Multi-Actuator CONtrol design for multi-body line-of-sight pointing of space missions". It is conducted at the University Carlos III of Madrid, Spain, and funded and supported by Airbus Defence and Space GmbH, Immenstaad, Germany. A. Marcos gladly acknowledges funding as Beatriz Galindo Distinguished Senior Researcher by the Spanish Government. In addition, his work has been supported by the Madrid Government (Comunidad de Madrid-Spain) under the Multiannual Agreement with UC3M in the line of "Research Funds for Beatriz Galindo Fellowships" (SPACEROBCON-CM-UC3M), and in the context of the V PRICIT (Regional Programme of Research and Technological Innovation). This work was further supported by the Space Agency of the German Aerospace Center (DLR, Deutsches Zentrum für Luft- und Raumfahrt e.V.) with means of the German Ministry of Economic Affairs and Climate Action under grant number 50 RK 2007. Funding for APC: Universidad Carlos III de Madrid (Read & Publish Agreement CRUE-CSIC 2023).

* Corresponding author.
E-mail address: aponche@pa.uc3m.es (A. Ponche).

https://doi.org/10.1016/j.actaastro.2023.03.020
Received 15 January 2023; Received in revised form 21 February 2023; Accepted 15 March 2023
Available online 17 March 2023

very quickly, and thus, the minimization of the time spent reorienting the spacecraft is the main driver. Performing autonomous slew maneuvers with attitude constraints requires computationally-efficient motion planning algorithms that can be run on-board in finite time. Currently, there are no efficient, simple and optimal autonomous solutions in the literature for such a MB/MA scientific observation space missions.

However, the problem of avoiding attitude zones while reorienting a spacecraft has been reasonably studied and can be divided in two main categories: geometric vector-based methods and potential-based methods. The former require a reference guidance profile and propose different autonomous avoidance methods: for example, Hablani developed a geometric optimized algorithm that prevents an instrument's boresight from entering a Sun exclusion zone while keeping an antenna's ground contact by computing intermediate tangential paths around the Sun exclusion cones [8]. Others, such as those based on escape torque algorithms [9], apply a counter-torque in addition to the control torque to avoid the forbidden zone. Although easy to implement, these solutions allow rotations about the instrument's boresight, which is not permitted for most space telescopes with partial sun-shields only. Additionally, these iterative approaches require fine tuning of the parameters and their convergence is not ensured, making them more appropriate for mission planning on ground only. On the other hand, potential-based methods reorient the spacecraft to the desired attitude by defining forbidden regions as high potential zones. Mc Innes [10] started with an analytical and on-board implementable solution, however it does not guarantee satisfaction of the avoidance constraints nor the possibility of expanding the constraint set, for example to rate and torque constraints or to a non-rotation about the boresight axis. The extension of this method to a convexified semi-definite programming approach of the problem [11,12] ensures convergence of the algorithm and a corresponding path-, time- and/or energy-optimal solution. However, these algorithms require an iterative solver and are usually run on ground. Addressing the aforementioned issues, this article presents a novel systematic and analytical guidance strategy for reorienting autonomously space observation spacecraft under Sun avoidance and attitude actuator constraints.

The article is organized as follows. After a comparison of industrial technical concepts for observation missions, Section 2 defines the guidance problem and presents a MB/MA benchmark mission. Two solutions to the guidance problem are proposed in Section 3. Thanks to the formulation of the spacecraft agility in terms of spacecraft torque and angular momentum envelopes, both solutions are constrained to the exact spacecraft angular momentum capacity, with the possibility of starting a maneuver with a non-zero initial angular momentum. First, a reference repointing guidance is derived based on an industrial state-of-practice slew guidance that satisfies attitude constraints. Then, a novel slew maneuver guidance approach, developed to minimize maneuver time, is formulated. In Section 4, the reduction of the maneuver time is verified via simulations, covering individual slew maneuvers as well as the simulation of a full realistic mission timeline.

2. Guidance problem and space observation benchmark mission

In this section, first the technical concepts for current and future space observation missions are reviewed. Then, the guidance problem arising in these missions is presented, followed by the description of the benchmark observation mission that is used in this article. The latter consists of a multi-body/multi-actuator spacecraft (Section 2.3.1) and a state-of-practice guidance solution (Section 2.3.2). This guidance will be used as a baseline for comparison, and it is detailed in Section 3.

2.1. Comparison of industrial concepts for space observation missions

The scientific goals of space observation missions have become increasingly demanding in terms of scientific availability and spacecraft agility requirements. A non-exhaustive list of such observation missions with individual requirements and attitude constraints is presented in Table 1. They are listed in chronological order of (planned) launch year, and the acronyms correspond to: Atmospheric Remote-sensing Infrared Exoplanet Large-survey (ARIEL), Advanced Telescope for High-ENergy Astrophysics (ATHENA), Hubble Space Telescope (HST), James Webb Space Telescope (JWST), Solar Dynamics Observatory (SDO), Solar Orbiter (SolO), and X-ray Multi-Mirror Mission (XMM).

Table 1
Space observation missions: requirements and attitude constraints.

Mission, launch year	Scientific availability	Slew rate [°/min]	Attitude constraints
HST, 1990	90% [3]	6 [3]	Depends on position on orbit and target [3]
Cassini, 1997	–	X_B, Y_B: 7.8 [13] Z_B: 15.6	Two Sun "keep-out zones" [13]
XMM, 1999	–	1.5 [14]	X_B: free [5] Y_B: ±20° Z_B: ±20°
SDO, 2010	95% [15]	Calibration: 18 [16]	X_B: free [6] Y_B: ±2.5° Z_B: ±2.5°
SolO, 2020	–	Calibration: 6 [17]	X_B: free Off-pointing from Sun line: ±6.5° [7]
JWST, 2021	70% [18]	1.6 [19]	X_B: free [4] Y_B: [-53; 0]° Z_B: ±5°
ARIEL, 2029	85%[20] (exp. 90%–92%)	4.5 [21]	X_B: free [20] Y_B: ±30° Z_B: ±6.75°
ATHENA, 2035	90% [1]	Nominal: 1 [22] Opp. target: 4 [1]	X_B: free [1] Y_B: ±34° Z_B: ±5°

In Table 1, the X_B-axis refers to the Sun-to-spacecraft direction, the Y_B-axis to the spacecraft transverse axis, and the Z_B-axis completes the right-handed orthogonal triad (for most of the missions, Y_B corresponds to the longitudinal axis of the solar array and Z_B to the spacecraft longitudinal/optical axis).

For all of the aforementioned missions, attitude exclusion zones are hard constraints whose violation would lead to the loss of the mission. For HST, XMM, JWST, ARIEL, and ATHENA, the attitude constraints are due to the high sensitivity of the scientific instruments and the necessity to prevent sunlight from entering their field of view. Concerning SDO and SolO, both shall remain pointing towards the Sun most of the time in order to stay within their thermal limits while the Sun-observing instruments take continuous measurements [6,7]. During calibration maneuvers they must keep the guide telescopes' field of view well outside a Sun exclusion zone [6].

Moreover, the scientific return of space observation missions can be improved by maximizing the image quality and resolution. For space telescopes, this is achieved by augmenting their objective aperture, and thus their focal length. This leads to designing massive space observatories, as shown in Table 2. XMM, SolO and ARIEL have a mass of 3,800 kg, 1,800 kg and 1,500 kg respectively, but not further information was found on their inertia properties.

For most of the reviewed missions, the overall science availability is expected to be larger than 85%. This means that at least 85% of the mission time shall be used for scientific observations, while other operational modes such as repointing maneuvers or orbit maintenance shall take at most 15% of the mission time. To maximize the time available for science observations, it is important to reduce the time spent reorienting the spacecraft. One of the main levers to achieve this reduction is to focus on the slew maneuvers between observations. All the reviewed missions use reaction wheels (RWs) as attitude actuators since they can store rotational energy by conserving angular momentum and can provide stability and counteract external disturbances by exchanging momentum with the satellite body.

Table 2
Space observation missions: spacecraft mass and inertia properties.

Mission	Mass [kg]	Moment of inertia [kg m^2]
HST	11,110	$\begin{bmatrix} 31,046 & & \\ & 77,217 & \\ & & 78,754 \end{bmatrix}$ [23]
Cassini	5,570	$\begin{bmatrix} 8,970 & & \\ & 9,230 & \\ & & 3,830 \end{bmatrix}$ [24]
SDO	3,000	$\begin{bmatrix} 1,923 & 45 & -4 \\ 45 & 3,640 & -5 \\ -4 & -5 & 3,000 \end{bmatrix}$ [25]
JWST	6,200	$\begin{bmatrix} 67,946 & -83 & 11,129 \\ -83 & 90,061 & 103 \\ 11,129 & 103 & 45,821 \end{bmatrix}$ [19]
ATHENA	8,000	$\begin{bmatrix} 200,000 & & \\ & 220,000 & \\ & & 20,000 \end{bmatrix}$ [26]

Table 3
Space observation missions: spacecraft reaction wheels characteristics.

Mission, Ref.	No. of RWs	RWs spatial configuration & spin axes direction	Nominal ang. mom. per RW, [Nms]	Nominal torque per RW, [mNm]
HST, [28,29]	4	Rectangular pyramid Elevation angle: 45° Spacing angle: 20°	250	820
Cassini, [13,30] [31]	3 +1	Regular pyramid Elevation angle: 54° Back-up, steerable	34	160
XMM, [32,33] [34]	4	2 symmetrical pairs: 3 active, 1 redundant Separation angles: -Elevation plane: 60° -Azimuth plane: 120°	40–45	248
SDO, [6,35]	4	Regular pyramid Elevation angle: 30°	70	250
JWST, [36–38]	6	Regular pyramid Elevation angle: 45°	68	75
ATHENA [1,38]	4	Regular pyramid Elevation angle: 75°	68	75

Thus, they result in high pointing accuracy and agility, and in addition can be used for reorienting the spacecraft between observations as well as precisely holding its attitude during the science mode. The attitude maneuver performances are directly driven by their maximal torque and angular momentum capacities. A typical reaction wheel array (RWA) is the regular pyramidal arrangement. This means that the pyramid's base is a regular polygon, its faces are isosceles triangles, and its apex is directly above the geometrical center of the base. This configuration enables to provide momentum capacity and torque in each of the three spacecraft axes and thus to ensure a three-axis pointing capability while being robust to any reaction wheel failure. Fixed in the body-frame, the reaction wheels are usually set up about the axis where the maximum momentum capacity is required for slew maneuvers. The reaction wheel equipment characteristics associated to the previous listed missions are presented in Table 3. SolO and ARIEL possess 4 reaction wheels [7,27], but no further information could be found on their configuration and characteristics.

To further improve the scientific performance, more and more space observatories are MB/MA spacecraft that possess several on-board instruments sharing one larger common mirror (instead of fixed, immobile instruments sharing individually or in parallel the same light focused by one or several immobile mirrors like HST [3] or XMM [39]). Examples are the recently launched JWST as well as the planned ATHENA and ARIEL telescopes. Both JWST and ATHENA are composed of a main body and a large movable primary mirror mounted on a hexapod mechanism [1,3]. For ARIEL, a short-range fine steering mechanism enables to change the focus of the secondary mirror [40]. The repointing maneuver of such spacecraft involves a slew maneuver performed with reaction wheels and a mirror steering towards the line of sight of the observing instrument. In the case of large moving mirrors, the spacecraft attitude can change significantly when the mirror is moved. When the target attitude is only known shortly before slewing the spacecraft and the observation is time-critical, reconstructing and updating in real-time the spacecraft attitude after the mirror motion enables to save time since the closed-loop control system does not have to correct the attitude error induced by the mirror motion.

Considering these requirements and constraints, a systematic, on-board computable and time-optimal guidance can be a considerable asset for MB/MA spacecraft.

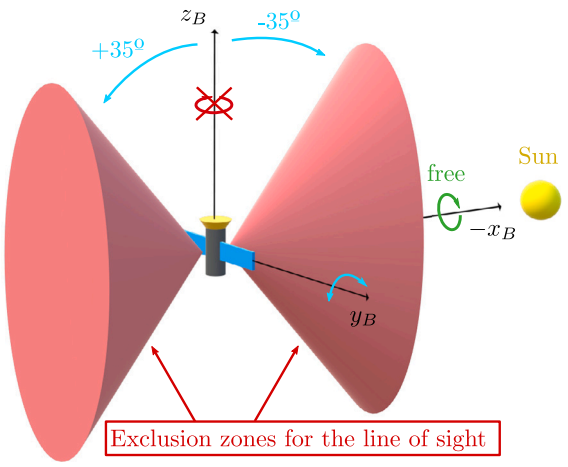

Fig. 1. Attitude constraints of guidance problem.

2.2. Guidance problem for autonomous and attitude-constrained maneuvers

The repointing guidance problem consists in performing autonomous, systematic, rest-to-rest (i.e. zero initial and final velocity) and time-efficient attitude-constrained repointing maneuvers. The attitude constraints for the benchmark mission are based on the ones from the XMM-Newton, JWST, ARIEL and ATHENA missions and are visualized in Fig. 1.

In order to prevent sunlight from entering the instruments' field of view, the line of sight (LoS) should stay within ±35° about the Y_B-axis. It should also not rotate about the Z_B-axis to keep the sun-facing side of the sun-shield correctly oriented. Finally, the rotation about the X_B-axis is unconstrained. These constraints provide an allowed pointing zone for the field of view, which is the complement of the two red exclusion cones represented on Fig. 1.

Moreover, the spacecraft should perform the repointing maneuvers by only commanding the target attitude with no other information from ground. Thus, the motion planning algorithms should be computationally efficient and run on-board in finite time. This is challenging since the guidance generation problem is almost always non-convex, which typically means that optimization algorithms are run on ground and guidance profiles are then uploaded to the spacecraft. No efficient and reliable on-board solution to this specific guidance problem is available in the literature to the best knowledge of the authors.

2.3. Benchmark mission

2.3.1. Multi-body/multi-actuator spacecraft

Driven by the examples from Section 2.1, a benchmark observation spacecraft was defined by Airbus, and is introduced and schematically

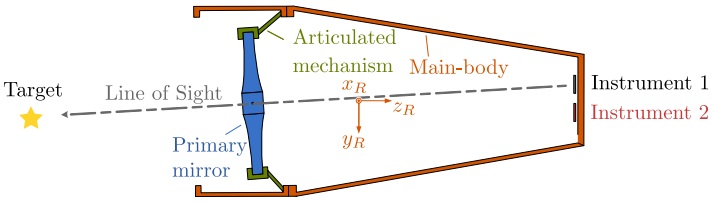

Fig. 2. Benchmark MB/MA spacecraft: line of sight direction and attitude reference frame [41]. (For interpretation of the references to color in this figure legend, the reader is referred to the web version of this article.)

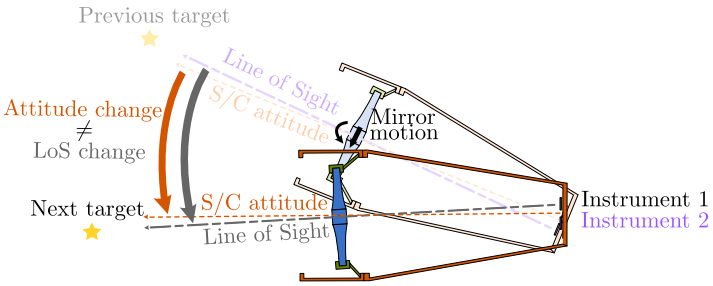

Fig. 3. S/C attitude change and LoS change during a repointing maneuver.

represented in Fig. 2. It is a MB/MA space telescope with a large primary mirror (in blue). The mirror is fixed on a six degree-of-freedom mechanism (in green). The mechanism can be used to: (1) rotate the mirror towards the line of sight (LoS) of the selected observation instrument, (2) set the correct focal length for the next observation, and (3) correct any possible misalignment between the instrument LoS and the mirror optical axis due to the thermal distortions of the telescope structure. Attitude control will be performed by reaction wheels, since they have been identified as typical attitude actuators for such spacecraft.

To discuss the attitude guidance problem, it is useful to define an attitude reference frame, and a coordinate system that is fixed to the spacecraft. The observation targets are defined in the attitude reference frame {R}. The axes are defined as follows:

- x_R is parallel to the Sun-spacecraft line, pointing away from the Sun
- y_R is the transverse axis, orthogonal to the Sun-LoS pointing plane
- z_R completes the right-handed orthogonal triad.

The body-fixed reference frame {B} consists of three orthogonal axes and has its origin at the spacecraft center of mass. The Z_B-axis is defined in such a way that it points in the same direction as the LoS, along the mirror perpendicular axis at its neutral position. The attitude is defined as the orientation of the coordinate frame {B} w.r.t the attitude reference frame {R}. In this article, the corresponding attitude angles are defined by the Tait-Bryan rotation sequence about the x-y-z axes: ϕ is the angle about x_R, θ is the angle about the rotated y-axis, and ψ is the angle about the twice rotated z-axis, i.e. $T_{BR} = T_3(\psi)T_2(\theta)T_1(\phi)$. Recalling the guidance problem from Section 2.2, since there is no rotation around Z_B-axis, the azimuth and elevation angles can be directly transposed into Tait-Bryan angles as follows: ϕ corresponds to the azimuth angle, θ corresponds to the elevation angle and ψ is 0 in the considered case.

2.3.2. State-of-practice guidance: Sequential single-axis maneuvers

Repointing the spacecraft between two observations involves an actuation of the articulated mechanism (to steer the mirror towards the instrument used for the next observation) and a spacecraft slew maneuver (to change the spacecraft attitude such that the line of sight points towards the new target). The difference between line of sight change and attitude change is illustrated in Fig. 3.

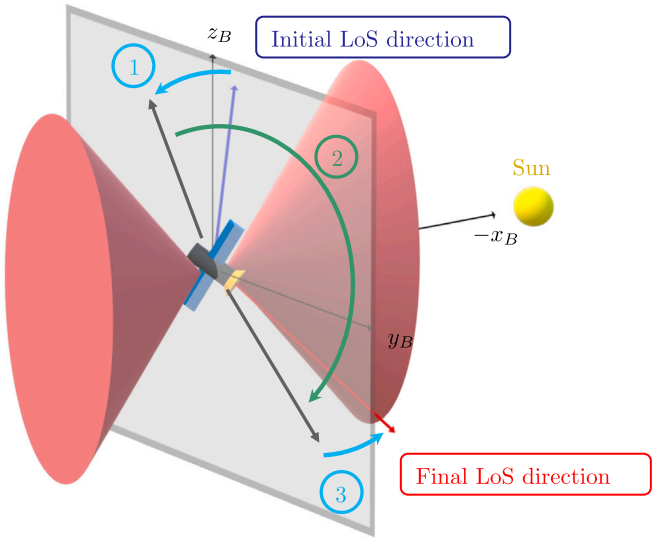

Fig. 4. State-of-practice: Sequential single-axis maneuvers.

Performing sequentially the mirror motion and the spacecraft slew maneuver enables to treat the spacecraft as a single-body during the slew maneuver, which reduces complexity in the repointing guidance architecture. Considering this, a typical industrial approach to perform the slew maneuver under attitude constraints consists in dividing the multi-axis maneuver into out-of-plane and in-plane single-axis maneuvers of the telescope line of sight [42–45]. In fact, using the $y_R z_R$-plane from Fig. 2, which is defined by its Sun-pointing normal and depicted in Fig. 4 for illustrative purposes, ensures that the attitude constraints for Sun avoidance are explicitly considered. A first rotation around the Y_B-axis of the spacecraft body frame cancels the initial elevation angle by bringing the spacecraft boresight into the azimuth plane (= $y_R z_R$-plane). Then, a second rotation is performed around the X_B-axis (azimuth), which will rotate the spacecraft boresight within the azimuth plane, and finally a third rotation around the Y_B-axis happens to lead the spacecraft boresight out of the azimuth plane to the new elevation angle at the final line of sight direction.

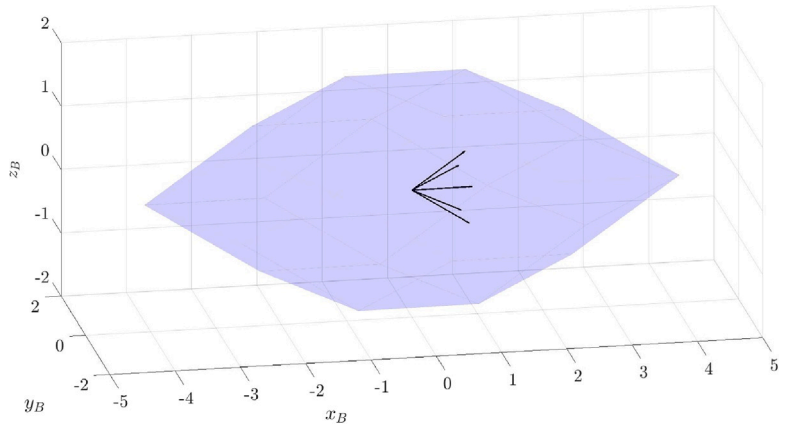

Fig. 5. Unit envelope for the considered RWA [41].

3. Solutions to the guidance problem

This section presents two solutions for performing autonomous and attitude-constrained maneuvers. The two guidance solutions are analytical, make use of these exact momentum boundaries in their computation, and satisfy the attitude constraints. Their difference lies in their torque profile and maneuver time. Thus, before presenting the guidance solutions, Section 3.1 formulates the spacecraft agility in terms of torque and angular momentum envelopes. The first solution (Section 3.2) corresponds to the state-of-practice presented in Section 2.3.2, while the second (Section 3.3) is the main contribution of this paper: it is a coupled-axis solution, time-optimal for a given spacecraft design and set of admissible observation targets.

3.1. Spacecraft torque and angular momentum capacity

3.1.1. Agility envelope when using identical reaction wheels

The angular momentum and torque capacity of a reaction wheel based attitude control system depends on the individual wheels' angular momentum and torque limits as well as on their orientation (i.e., the RWA architecture). For an N-reaction wheel array, the wheels' torques and angular momenta are mapped to the spacecraft's body axes by the alignment matrix

$$A_{\mathrm{RW}\to B} = \begin{bmatrix} \mathbf{u}_1 & \cdots & \mathbf{u}_N \end{bmatrix} \tag{1}$$

where $\mathbf{u}_1, \ldots, \mathbf{u}_N$ are the reaction wheels' spin axes expressed in the body frame.

The angular momentum envelope of the RWA can then be formulated mathematically as

$$\mathbf{h}_{\mathrm{RW}} = A_{\mathrm{RW}\to B}\, \mathbf{h}_{\mathrm{w}}, \quad |h_{\mathrm{w},i}| \le h_{\max}, \quad i = 1, \ldots, N \tag{2}$$

where $\mathbf{h}_{\mathrm{RW}} \in \mathbb{R}^3$ is the angular momentum in the body frame, $\mathbf{h}_{\mathrm{w}} \in \mathbb{R}^N$ collects the individual wheels' angular momenta, and $h_{\max}$ is the maximum angular momentum per reaction wheel (assumed equal for all wheels). Eq. (2) describes a zonotope and it can be constructed using e.g. the algorithm proposed in [46].

As an example, Fig. 5 shows the angular momentum envelope of a symmetrical five reaction wheel array with the following alignment matrix

$$A_{RW\to B} = \begin{bmatrix} \sin\alpha & \sin\alpha & \sin\alpha & \sin\alpha & \sin\alpha \\ 0 & \sin\beta\cos\alpha & \sin(2\beta)\cos\alpha & \sin(3\beta)\cos\alpha & \sin(4\beta)\cos\alpha \\ \cos\alpha & \cos\beta\cos\alpha & \cos(2\beta)\cos\alpha & \cos(3\beta)\cos\alpha & \cos(4\beta)\cos\alpha \end{bmatrix} \tag{3}$$

and the alignment angles α=55° and β=360°/5=72°.

The axes are normalized with respect to $h_{\max}$. Each facet of the zonotope corresponds to a saturated angular momentum of all but the two reaction wheels whose spin axes are parallel to the facet. In the same manner, each edge represents a saturated angular momentum of all wheels except the one whose spin axis is parallel to that edge. The torque envelope can be computed analogously by replacing all angular momenta in Eq. (2) by the corresponding torque values.

The torque and angular momentum envelopes of a reaction wheel array have the same shape and only differ by a scalar ratio, which has been named Ka by [47]. In the following, we will slightly generalize this ratio by considering the allocation rates α_h and α_T of the RWA angular momentum and torque, respectively, to the feed-forward guidance. Setting $\alpha_T < 1$, it retains some torque capacity for feedback control during the slew maneuver. In addition, setting $\alpha_h < 1$ reserves some angular momentum capacity for accumulated disturbances. The performance ratio between angular momentum and torque is thus defined as:

$$K_{T\to h} = \frac{\alpha_h\, h_{\max}}{\alpha_T\, T_{\max}}. \tag{4}$$

3.1.2. Useful envelope properties and angular momentum bias

Moreover, an additional part of the global angular momentum storage capability is reserved for momentum accumulation, which is mainly caused by the solar radiation pressure disturbing torque for most of the space observation missions. For this reason, it is very likely that a slew maneuver starts with a non-zero angular momentum storage. This initial condition must be considered when building the angular momentum envelope. In the Markley's algorithm [46], a maximum angular momentum capacity C_i is attributed to each envelope's facet i, in the direction of its normal vector $\mathbf{n}_i$. This net angular momentum is computed by adding the projections of each reaction wheel capacity in the direction of this normal vector. Instead of attributing this maximum capacity C_i to each facet, a current available capacity h_i is introduced. It consists in subtracting the initial angular momentum from the maximal one for each facet i. To do so, the initial angular momentum ($\mathbf{h}_0$) is projected on the facet's normal unit vector ($\mathbf{n}_i$) and subtracted from its maximum angular momentum capacity C_i (see Eq. (5)). The case $h_i > C_i$ is possible, i.e. angular momentum bias may increase agility for some maneuvers.

$$h_i = C_i - (\mathbf{h}_0 \cdot \mathbf{n}_i) \tag{5}$$

Thanks to the geometric properties of the envelopes constructed in the proposed form, it is possible to perform analytical checks by computing the distance ratio between the vector and the envelope in order to verify if a vector of interest is within the envelope, on its limit, or violating it. The method is derived for the angular momentum envelope, but the same checks can be done with the torque envelope.

For all the facets of the angular momentum envelope, the vector of interest $\mathbf{v}$ is projected on the normal unit vector ($\mathbf{n}_i$) of each facet i:

$$\mathbf{p}_{\mathbf{n}_i}(\mathbf{v}) = (\mathbf{v} \cdot \mathbf{n}_i)\, \mathbf{n}_i \tag{6}$$

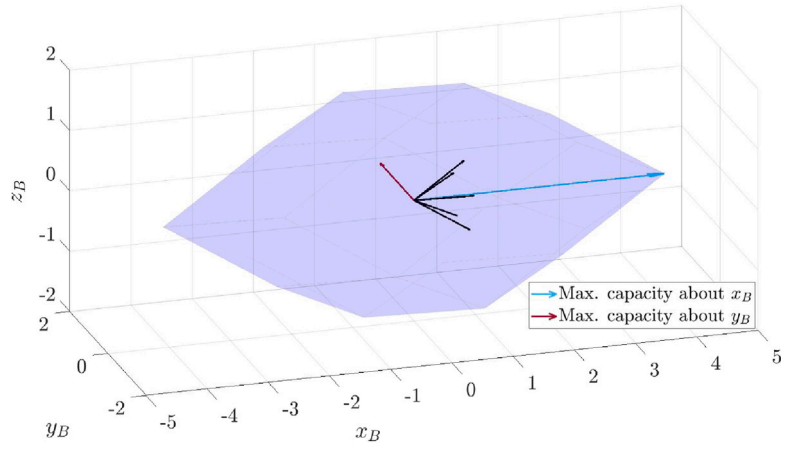

Fig. 6. X_B and Y_B-axis capacities for the considered RWA.

Moreover, each facet i is at the maximum capacity distance h_i from the center. Thus, dividing each projected vector length by this maximum capacity will provide the distance ratio r_i between the projected vector on facet i and the facet i maximum capacity:

$$r_i = \frac{\|\mathbf{p}_{\mathbf{n}_i}(\mathbf{v})\|}{h_i} \tag{7}$$

The highest ratio r_i over all facets i represents the multiplying factor by which the input vector needs to be divided to exactly reach the angular momentum envelope:

$$r_h = \max_{i \in [\![1; N_{\text{facets}}]\!]} r_i \tag{8}$$

This ratio r can be seen as a angular momentum norm, analogous to the torque norm introduced in [48], whose value leads to the following useful property:

$$\begin{cases} r_h < 1 \Leftrightarrow \mathbf{v} \text{ is inside the angular momentum envelope} \\ r_h = 1 \Leftrightarrow \mathbf{v} \text{ reaches the angular momentum envelope} \\ r_h > 1 \Leftrightarrow \mathbf{v} \text{ crosses the angular momentum envelope.} \end{cases} \tag{9}$$

This ratio can be used for checking the violation/margin of an input vector, or it can be used to find the maximum torque and angular momentum capacities about a direction of interest. This will be used in Section 3.2 to compute the envelope-constrained reference guidance, and in Section 3.3.1 to compute the optimal maneuver times for the proposed guidance approach.

3.2. Reference solution: Envelope-constrained single-axis guidance

In this section, a reference repointing guidance between two observations is presented. It corresponds to the state-of-practice presented in Section 2.3.2, constrained to the exact spacecraft torque and momentum envelopes.

As explained in Section 2.3.2, any multi-axis slew maneuver is divided into three consecutive single-axis maneuvers in order to satisfy the attitude constraints. The spacecraft available torque and angular momentum about the X_B and Y_B axes are needed to compute the torque and angular momentum profiles for each sub-maneuver. To do so, the envelope properties from Section 3.1.2 are used to compute the capacities about these two axes of interest to reach the envelope. For the exemplary five-RW array introduced above, these capacities are represented on the unit envelope in Fig. 6.

The entire available angular momentum about the X_B and Y_B axes can be used since only one axis is used by each sub-maneuver. The maximum acceleration and velocity per axis are directly computed from these available angular momentum and torque. The single-axis maneuver times and acceleration profiles are obtained by integrating twice the available acceleration about the axis in question, considering the initial and final angles conditions about the axis and checking that the maximum velocity is not violated. If violated, the velocity profile is restricted and a coast-phase corresponding to a phase with a null-acceleration and thus a velocity plateau is added in order to reach the expected angle about the axis. Simulation results for this reference solution are shown in the dedicated results of Section 4.2.1.

3.3. A novel coupled-axis guidance solution

The established single-axis guidance approach is a robust solution that allows to satisfy the attitude constraints while being easy to implement on-board and capable of operating autonomously. However, this approach is not the most time efficient since three consecutive sub-maneuvers (and thus six acceleration and deceleration phases) are performed for each slew maneuver. Thus, a novel coupled-axis guidance solution requiring only one acceleration and one deceleration phase, and satisfying the attitude requirements, is proposed in this section. For any given rest-to-rest slew maneuver, the optimal maneuver time is retrieved from the agility envelopes, and the slew profile is computed analytically.

3.3.1. Optimal maneuver time computation

This section presents the method to compute the optimal maneuver time for the total slew angle $\boldsymbol{\Delta}_{angle}$. Starting from this slew angle, the minimal actuation time, i.e. using all the available torque and disregarding the angular momentum limitation, is first computed. Then it is checked whether actuating the spacecraft during this minimal time at maximum torque leads to a violation of the available angular momentum. The cases without and with violation are handled later in this section, and the corresponding optimal maneuver times are provided in each of the cases. Quantities in the momentum domain are used in this section since the momentum envelopes are available. The correspondence between the spacecraft momentum domain capacity and its angular domain limits is shown in Fig. 7.

The slew angle $\boldsymbol{\Delta}_{angle}$ counterpart in the momentum domain is noted $\boldsymbol{\Delta}_p$ and is computed as in Eq. (10). This quantity is not physically meaningful but will be helpful since the angular momentum and torque envelopes are already available.

$$\boldsymbol{\Delta}_p = \mathbf{J}_{SC} \cdot \boldsymbol{\Delta}_{angle} \tag{10}$$

Consider the ratio $K_{T \to \boldsymbol{\Delta}_p}$ by which the vector $\boldsymbol{\Delta}_p$ needs to be multiplied so that it reaches the torque envelope (Fig. 8). This ratio corresponds to the ratio r from Eq. (9) when the method is applied to the input vector $\boldsymbol{\Delta}_p$ and the torque envelope. This ratio is of unit

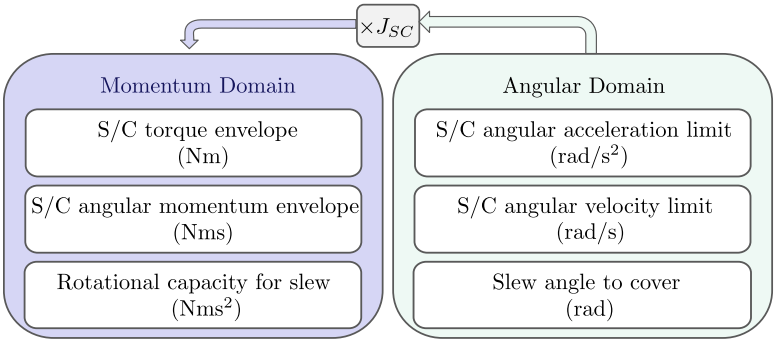

Fig. 7. Transformation between angular and momentum domains.

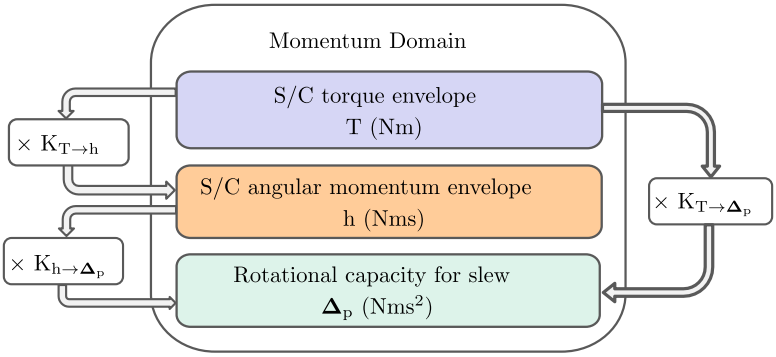

Fig. 8. Analytical computation of optimal rest-to-rest maneuver time.

Table 4
Space observation missions: RW angular momentum to torque ratio $K_{T\to h}$.

Mission	HST	Cassini	XMM	SDO	JWST	ATHENA
$K_{T\to h}$, [s] (see Eq. (4))	305	213	161–181	280	907	907

s^2 and its square root represents the acceleration time of a bang–bang maneuver that covers $\boldsymbol{\Delta}_{angle}$ using the maximum torque.

$$t_{min} = \sqrt{K_{T\to\boldsymbol{\Delta}_p}} \tag{11}$$

Now it needs to be checked whether actuating the reaction wheels during this time t_{min} at maximum torque leads to an angular momentum violation. As explained in Section 3.1, the ratio $K_{T\to h}$ between the torque and angular momentum envelopes is known and fixed. It can be seen as a performance indicator, representing the time required to reach the maximum angular momentum when actuating at the maximum torque. Table 4 provides an order of magnitude of this ratio for the reviewed missions. Thus, comparing the optimal time t_{min} to the ratio $K_{T\to h}$ enables to check whether the angular momentum is violated for the maneuver to perform.

3.3.1.1 Optimal maneuver time for torque-constrained maneuver In the case $\boldsymbol{t_{min} < K_{T\to h}}$, actuating the spacecraft at maximum torque during t_{min} will not lead to any angular momentum violation. In practice, a bang–bang maneuver can be performed, which means that the spacecraft can be accelerated (first bang phase) and decelerated (second bang phase) at maximum acceleration without reaching the maximum angular rates. In this case, the optimal maneuver time is directly deduced from the minimal actuation time as follows:

$$t_{man} = 2\ t_{min} \tag{12}$$

3.3.1.2 Optimal maneuver time for angular momentum-constrained maneuver In the case $\boldsymbol{t_{min} > K_{T\to h}}$, the maximum angular momentum is reached if the spacecraft is actuated at maximum torque during t_{min}. The spacecraft can be only actuated at maximum torque during $K_{T\to h}$, which is not enough to reach $\boldsymbol{\Delta}_p$, and thus cover the slew angle $\boldsymbol{\Delta}_{angle}$. The remaining time needed to reach $\boldsymbol{\Delta}_p$ at maximum angular momentum must be added. This corresponds to the time ratio $K_{h\to\boldsymbol{\Delta}_p}$ between $\boldsymbol{\Delta}_p$ and the angular momentum envelope. It is computed using the method from Section 3.1 and corresponds to the ratio r from Eq. (9) when the method is applied to the input vector $\boldsymbol{\Delta}_p$ and the angular momentum envelope. Unlike the ratio $K_{T\to h}$, $K_{h\to\boldsymbol{\Delta}_p}$ depends on the reaction wheels configuration and the maneuver to perform. It represents the minimum time to reach the angular momentum envelope in $\boldsymbol{\Delta}_p$ direction, and it will be different for each maneuver. In this case, the maneuver time will be the sum of the time needed to reach the maximum angular momentum at maximum torque, and the remaining time needed to reach at maximum angular momentum, i.e.:

$$t_{man} = K_{T\to h} + K_{h\to\boldsymbol{\Delta}_p} \tag{13}$$

In practice, the spacecraft is first actuated at maximum torque until reaching the angular momentum limit at $K_{T\to h}$. Then it will be slewed at constant (and maximum) angular momentum during the coasting time, before being decelerated at maximum torque until achieving the desired attitude during $K_{T\to h}$. Such a maneuver is called bang-coast-bang maneuver, where the coast time t_{coast} is computed as in Eq. (14). Note that Eqs. (13) and (14) are equivalent.

$$t_{man} = 2\ K_{T\to h} + t_{coast}, \text{ with } t_{coast} = K_{h\to\boldsymbol{\Delta}_p} - K_{T\to h} \tag{14}$$

In both cases, the optimal maneuver times are known in $\boldsymbol{\Delta}_p$ direction. Now, the slew angles guidance profiles satisfying the attitude constraints must be computed from the available torque and angular momentum. This will be the purpose of the next section, where the torque-limited (bang–bang torque profile) and the angular momentum-limited (bang-coast-bang torque profile) maneuver computations will be derived.

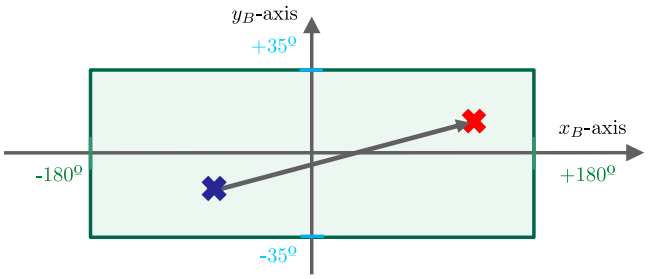

Fig. 9. Convex permissible attitude zone.

3.3.2 Analytical envelope-constrained guidance computation

The proposed guidance principle is to generate a continuous path that enables to slew from permissible initial angles to permissible final angles while satisfying the attitude constraints at each time step.

Recalling the guidance problem from Fig. 1 in Section 2.2, the permissible zone for the line of sight is the complement of the two exclusions cones, and can be defined from the azimuth/elevation restrictions: in the orthogonal coordinate system made by the X_B-axis and the Y_B-axis, it is a rectangle spanning ±180° on the X_B-axis and ±35° on the Y_B-axis, and thus a convex set. By definition, a convex region is a region where any line segment joining any two points from the region entirely lies within the region, i.e. every point on the line segment is also within the region (see [49]). This means that line segments joining any initial angles in the permissible zone and any final angles in the permissible zone lie within the permissible zone (see Fig. 9).

Therefore, it will be possible to find a slew maneuver from any initial Euler angles (with the subscript i) in the zone to any final Euler angles (with the subscript f) in the zone, within this zone:

$$\begin{cases} (\phi_i \quad \theta_i \quad \psi_i) & = (\text{azimuth}_i \quad \text{elevation}_i \quad 0) \\ (\phi_f \quad \theta_f \quad \psi_f) & = (\text{azimuth}_f \quad \text{elevation}_f \quad 0). \end{cases} \tag{15}$$

Since a rest-to-rest maneuver starts and ends with zero velocity, the corresponding initial and final Euler rates are zero. This implies that the acceleration and deceleration must be performed using the same amount of time. For each slew maneuver, the optimal maneuver time has been computed from the angular momentum and torque envelopes in Section 3.3.1. In the end, this introduction has proven that a slew maneuver guidance profile combining the X_B- and Y_B- axes can be generated. The bang–bang (i.e. torque-limited) and bang-coast-bang (i.e. angular momentum-limited) guidance profiles are computed hereafter.

3.3.2.1 Bang–bang maneuver profile This section presents the case where the angular momentum constraint is not violated, and thus a bang–bang torque profile can be generated. It consists in accelerating and decelerating the spacecraft about the first two Euler axes simultaneously. In order to generate the Euler angles profiles for the maneuver, the available acceleration about the first two Euler axes is needed. The available torque $\mathbf{T}_{max}$ in the $\boldsymbol{\Delta}_p$ direction is computed using the envelope geometry from Section 3.1, and the available acceleration is computed from the available torque as follows:

$$\boldsymbol{\alpha} = \boldsymbol{J}_{SC}^{-1} \cdot \boldsymbol{T}_{max} \tag{16}$$

The slew angle vector $\boldsymbol{\Delta}_{angle}$ to cover during the maneuver corresponds to specific initial and final Euler angles as introduced in Eq. (15).

Thus, considering that the available acceleration per Euler axis is:

$$\boldsymbol{\alpha} = \begin{bmatrix} \alpha_\phi \\ \alpha_\theta \\ \alpha_\psi \end{bmatrix}, \tag{17}$$

the acceleration times per Euler axis t_θ and t_ϕ can be computed from the individual available accelerations per Euler axis as follows:

$$t_\phi = \sqrt{\frac{\phi_f - \phi_i}{\alpha_\phi}} \quad ; \quad t_\theta = \sqrt{\frac{\theta_f - \theta_i}{\alpha_\theta}} \tag{18}$$

Since $\boldsymbol{\alpha}$ is computed from $\mathbf{T}_{max}$, the optimal time t_{min} computed in Eq. (11) corresponds to the larger of t_θ and t_ϕ. Indeed, t_{min} is by definition the biggest ratio among the two axes between the available torque $\mathbf{T}_{max}$ and the $\boldsymbol{\Delta}_p$ direction. Thus, it is also the biggest ratio among the two axes between the available acceleration per axis and the angle per axis in the angular domain.

As an example, the case $t_\theta < t_\phi$ is considered, (but it is noted that it is the same reasoning for $t_\phi < t_\theta$). In this example, the acceleration time for the maneuver is $t_{min} = t_\phi$. This means that the acceleration about the y-axis that is going to be used for the maneuver will be lower than the available one for the y-axis, since more time is available to perform the y-axis Euler rotation. The scaled acceleration about the y-axis is computed as follows:

$$\alpha_{\theta,\text{scaled}} = \frac{\theta_f - \theta_i}{{t_\phi}^2} = \alpha_\phi \frac{\theta_f - \theta_i}{\phi_f - \phi_i} \tag{19}$$

By integrating the accelerations twice, and considering that the initial and final velocities are zero (rest-to-rest maneuver) as well as the continuity of $\theta(t)$ at $t = t_{min}$, the expression of θ in function of time during the maneuver can be expressed.

$$\phi(t) = \begin{cases} \phi_i + \alpha_\phi \dfrac{t^2}{2} & \forall t \in [0; t_{min}] \\ \phi_i - \alpha_\phi {t_\phi}^2 + 2\alpha_\phi t_\phi t - \alpha_\phi \dfrac{t^2}{2} & \forall t \in [t_{min}; 2t_{min}] \end{cases} \tag{20}$$

The same profile is valid for the θ angle, using $\alpha_{\theta,\text{scaled}}$ instead of α_θ as acceleration about the y-axis.

In the same manner, if $t_\phi < t_\theta$, then $t_{min} = t_\theta$ and the scaled acceleration about the x-axis is:

$$\alpha_{\phi,\text{scaled}} = \alpha_\theta \frac{\phi_f - \phi_i}{\theta_f - \theta_i} \tag{21}$$

3.3.2.2 Bang-coast-bang maneuver profile This section presents the case where the angular momentum constraint would be violated in case of a bang–bang maneuver. To satisfy the angular momentum constraint defined by the momentum envelope, the time of the acceleration and deceleration phases must be reduced to accumulate less angular momentum than the maximum one.

As presented in Section 3.3.1, the spacecraft can be accelerated and decelerated at maximum torque during the maximum time $K_{T\to h}$ before reaching the maximum angular momentum value. Then, the coasting time $K_{h\to\boldsymbol{\Delta}_p}$ is the remaining time to reach $\boldsymbol{\Delta}_P$ at maximum angular momentum.

Thus, the two bang phases (acceleration and deceleration phases) can last a maximum time of $t_{bang} = K_{T\to h}$, and the coast time will last $t_{coast} = K_{T\to h} - K_{h\to\boldsymbol{\Delta}_p}$.

The guidance formulas from the previous case are extended to compute the coast time analytically. The new acceleration profile will be integrated twice to retrieve the new velocity and angle profiles. The initial and final conditions are unchanged. The coast-phase, lasting t_{coast}, corresponds to a null-acceleration and a velocity plateau. For easier reading, the intervals will be renamed as hereafter:

$$\begin{cases} \mathrm{I}^1_{bang} = [0; t_{bang}] \\ \mathrm{I}_{coast} = [t_{bang}; t_{bang} + t_{coast}] \\ \mathrm{I}^2_{bang} = [t_{bang} + t_{coast}; 2t_{bang} + t_{coast}] \end{cases} \tag{22}$$

Augmented with the coast phase, the acceleration about the x-axis is now expressed as in Eq. (23).

$$\ddot{\phi}(t) = \begin{cases} +\alpha_\phi & \forall t \in \mathrm{I}^1_{bang} \\ 0 & \forall t \in \mathrm{I}_{coast} \\ -\alpha_\phi & \forall t \in \mathrm{I}^2_{bang} \end{cases} \tag{23}$$

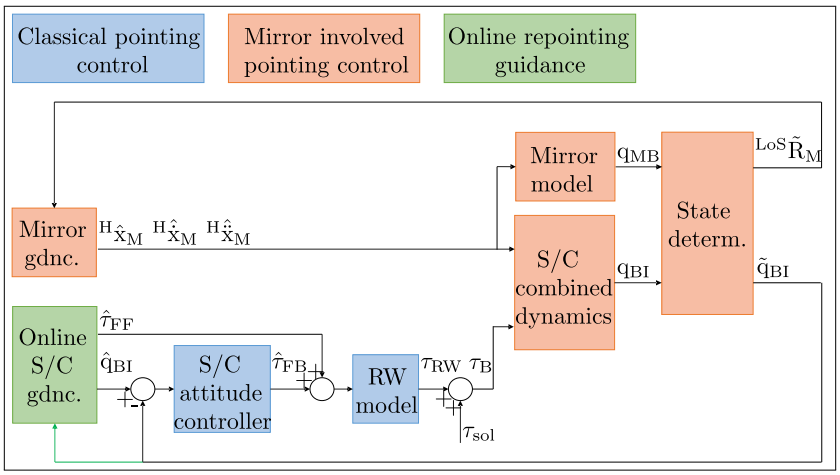

Fig. 10. Pointing control architecture for online guidance computation [50].

By integrating Eq. (23) twice and by using the continuity arguments at $t = t_{bang}$ and $t = t_{bang} + t_{coast}$, the angle profile can be expressed as follows:

$$\phi(t) = \begin{cases} \phi_i + \alpha_\phi \, t^2/2 & \forall t \in \mathrm{I}^1_{bang} \\ \phi_i - \alpha_\phi \, \dfrac{t^2_{bang}}{2} + \alpha_\phi \, t_{bang} \, t & \forall t \in \mathrm{I}_{coast} \\ \theta_i - \alpha_\phi \left(t_{bang} \, t_{coast} + \dfrac{t^2_{coast}}{2} \right) + \alpha_\phi \, t \left(2t_{bang} + t_{coast} - \dfrac{t}{2} \right) & \forall t \in \mathrm{I}^2_{bang} \end{cases} \tag{24}$$

The same reasoning applies for θ about the y-axis.

4 Simulation results

In this section, the simulation environment used to validate and compare the two guidance approaches is first presented (Section 4.1), followed by the simulation results for the reference (Section 4.2.1) and the novel (Section 4.2.2) guidance solutions and their comparison (Section 4.3).

4.1 Simulation environment for multi-body/multi-actuator online repointing

In this section, a pointing control architecture enabling an autonomous line of sight guidance and control of the multi-body spacecraft/multi-actuator benchmark spacecraft is presented. The spacecraft repointing, i.e. the mirror motion followed by the spacecraft slew maneuver, is performed autonomously. The attitude sensor is supposed to be mounted on the mirror to dispose of a mirror inertial measure so that the mirror can always be aligned with the target. In this case, no direct measurement provides the spacecraft attitude (i.e. the spacecraft main-body orientation with respect to the inertial frame). It is reconstructed from the knowledge of the mirror inertial measure and the knowledge of the mirror position and orientation w.r.t the spacecraft body. Hence, if the mirror is moved before the spacecraft slew maneuver, the additional spacecraft attitude changes brought by the mirror motion can be corrected during the slew maneuver (see [1]). The spacecraft slew guidance can then be computed online after the mirror motion. A pointing control architecture suiting this repointing strategy was proposed in a previous work on the investigation of MB/MA methods [50], and is recalled in Fig. 10.

The guidance strategies presented in this paper (see Sections 3.2 and 3.3) are implemented and verified using a high-fidelity, non-linear simulator provided by Airbus [42] and further developed to suit the online architecture from Fig. 10. The agility envelopes presented in Section 3.1 have also been implemented in the simulator to have access to the exact torque and angular momentum limitations of the spacecraft when computing the guidance solutions. They are simulated in the time-domain and in closed-loop with a preliminary attitude controller designed for a single-body spacecraft (see precision pointing H_∞ closed-loop shaping framework in [51]). As a reference repointing maneuver, a slew from an initial azimuth and elevation of (0°, 30°) to (120°, 20°) is considered, which is preceded by a mirror motion.

4.2 Simulation results and comparison

4.2.1 Reference single-axis guidance

In the simulation environment, the spacecraft attitude is expressed through quaternions (for the attitude integration) or Euler angles (for the guidance) from the attitude reference frame to the body-fixed frame. The implementation of the single-axis reference guidance in the simulation environment is fairly simple since each sub-maneuver is performed about the X_B or the Y_B spacecraft axes, and thus only one of the three Tait-Bryan angles is involved per sub-maneuver. This means that the Euler rates and accelerations are equal to the Body velocity and acceleration for each sub-maneuver.

The guided torque corresponding to the reference repointing maneuver is presented in Fig. 11 using normalized time (x-axis) and torque (y-axis) values. It is computed using the reaction wheel array (RWA) from Eq. (3) and the exact torque and angular momentum envelopes. It is composed of a first bang–bang sub-maneuver about the Y_B-axis (from 0.16 to 0.38 in the normalized time axis), a second bang-coast-bang maneuver about the X_B-axis (from 0.38 to 0.80 in the normalized time axis) and a third bang–bang maneuver about the Y_B-axis (from 0.80 to 1 in the normalized time axis).

Fig. 12 shows the resulting time-domain response of the attitude angles in body-frame {B} from the closed-loop, nonlinear simulation of the single-axis guidance. As described above, the slew maneuver components (named as SC Man. 1, 2, and 3 in Fig. 12) performed after the mirror motion ensure that the attitude constraints for Sun avoidance are explicitly considered.

A very important aspect in any project is the visualization of the gains. In order to compare the maneuver times between the different slew maneuvers, a pixel map is shown in Fig. 13. Starting from extreme initial angles in body-frame (azimuth: −180°, elevation: −35°), the map covers the whole set of allowed final angles.

Each pixel corresponds to a normalized maneuver time with respect to the maximal maneuver time for the covered azimuth (X_B-axis) and

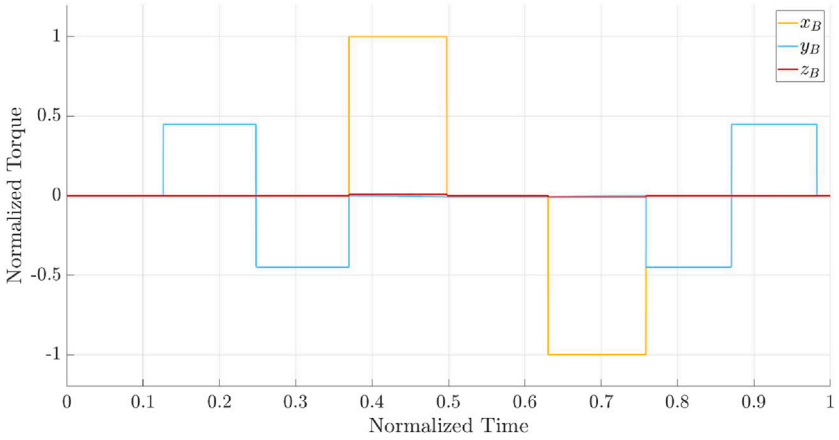

Fig. 11. Guided torque from envelope-constrained single-axis guidance in {B}-frame w.r.t {R}-frame [41].

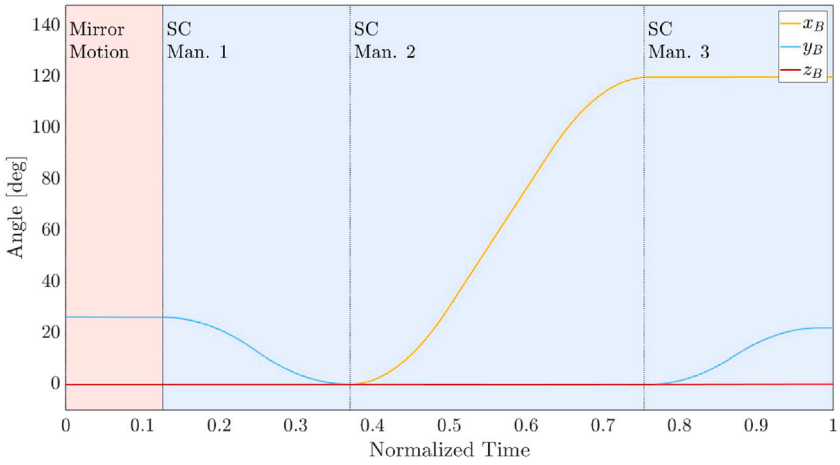

Fig. 12. S/C Euler angles from single-axis guidance in {B}-frame w.r.t {R}-frame [41].

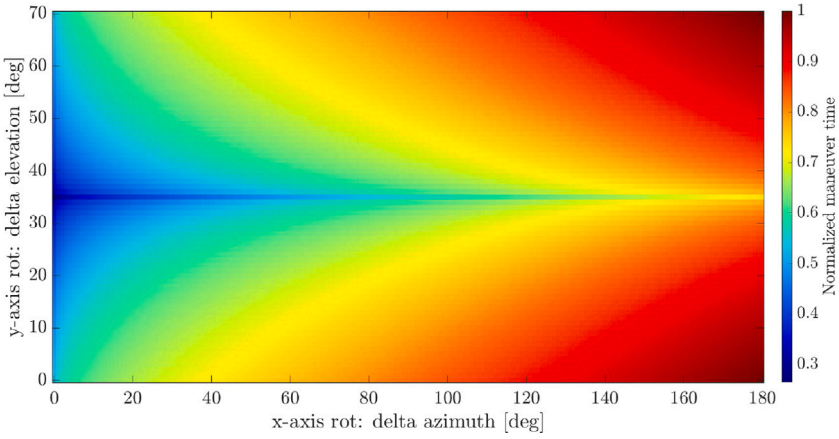

Fig. 13. Maneuver time pixel map for the envelope-constrained single-axis guidance [41]. (For interpretation of the references to color in this figure legend, the reader is referred to the web version of this article.)

elevation ranges (Y_B-axis). The map represents a maximum azimuth range of 180°, as the spacecraft can be rotated without constraint around the X_B-axis, leading to a maximum rotation of 180°. On the other hand, the time-map is symmetrical about the Y_B-axis because of the three consecutive generated maneuvers. As for the previous figure, the maneuver times have been normalized, on the right vertical bar.

4.2.2 Novel coupled-axis guidance

The implementation of the coupled-axis guidance in the simulation environment is not as straightforward as the reference guidance. Indeed, in this case each maneuver combines two of the Euler accelerations ($\ddot{\phi}\ \ddot{\theta}\ \ddot{\psi}$), rates ($\dot{\phi}\ \dot{\theta}\ \dot{\psi}$), and angles ($\phi\ \theta\ \psi$). This means that they follow individual coordinate rotations according to the Euler sequence.

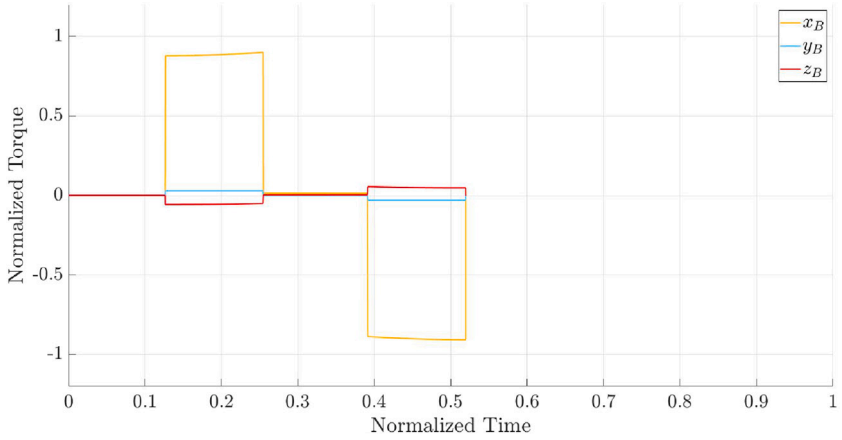

Fig. 14. Commanded torque from coupled-axis guidance in {B}-frame w.r.t. {R}-frame [41].

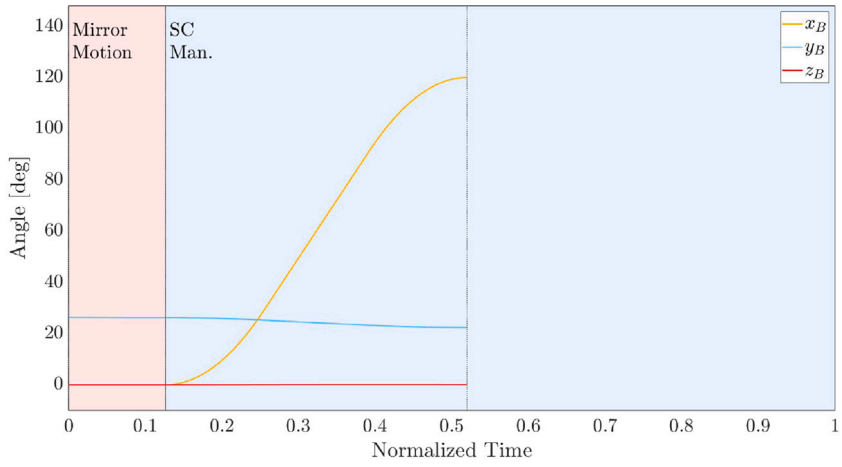

Fig. 15. S/C Euler angles from coupled-axis guidance in {B}-frame w.r.t. {R}-frame [41].

The spacecraft body-fixed quantities are obtained by expressing these Euler quantities in the body coordinate frame, using Euler-to-Body kinematic relationships [52,53].

The reference repointing maneuver is simulated using the proposed coupled-axis guidance, and the results are presented in Body-frame using the above transformation process.

Fig. 14 shows the resulting normalized torques versus normalized times. Comparing Fig. 14 with Fig. 11 (resulting from the single-axis guidance), it is seen that the proposed guidance is twice as fast as the single-axis one. It is also seen that the resulting guidance is a simultaneous combination of bang-coast-bang maneuvers about the three body axes.

Fig. 15 (the equivalent of Fig. 12), shows the resulting time-domain response of the Euler angles from the closed-loop nonlinear simulation of the coupled-axis guidance.

Finally, for ease of comparison to the single-axis guidance, Fig. 16 depicts the resulting pixel map obtained with the coupled-axis approach. Comparing it to Fig. 13 shows the advantages of the latter over the single-axis guidance. The clear difference comes from the fact that the maneuvers are performed in parallel in the coupled-axis case, and not subsequently.

4.3 Comparison of the simulation results

For a better comparison of the approaches, a pixel map as those in Figs. 13 and 16 can be obtained but, using for the pixels' colors, the ratio between their corresponding normalized maneuver times (see the different colormap legend on the right of the figure). The map on Fig. 17 represents the ratio of coupled-axis to single-axis maneuver times. Since the ratio is always lower than (or for one case equal to) one, the maneuver generated from the coupled-axis guidance is always faster than (or for one case as fast as) that with the single-axis approach. There is only one case for which the ratio is one: the maneuver from (azimuth: −180°, elevation: −35°) to (azimuth: −180°, elevation: 0°). In this specific case the same maneuver is generated by both methods. There are improvements of more than 50% in the maneuver time for almost half of the cases. This corresponds to the zones where the ratio is smaller than 0.5, i.e. the blue-to-green region at the bottom of the map. The average ratio of this test case is 0.55, which means that the maneuver time generated with the coupled-axis guidance is in average 1.8 times faster than the one generated with the single-axis guidance.

It is highlighted that the maneuver time for both guidance solutions could be further reduced by finding a RWA fitting better the guidance problem. Indeed, the elevation angle α presented in Section 3.1 was found in an iteration process and could be optimized (see [46,54]). This is why the current guidance solution is time-optimal for a given spacecraft design, i.e. a given RWA.

To assess the proposed approach at mission level, it was implemented in an Airbus in-house mission timeline simulator. This simulation environment covers all relevant mission phases such as scientific observations, the time needed for instrument switching, orbit maintenance maneuvers, RWA desaturation, etc. According to preliminary results, the developed coupled-axis guidance could increase the scientific availability from 89% [55] to 91%, which is a reduction of more than 20% of the mission time that is *not* available for scientific observations.

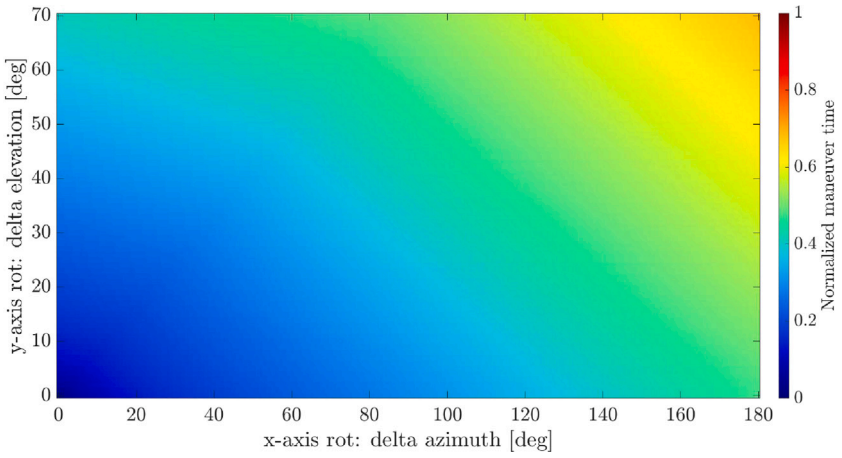

Fig. 16. Maneuver time pixel map for the envelope-constrained coupled-axis guidance [41]. (For interpretation of the references to color in this figure legend, the reader is referred to the web version of this article.)

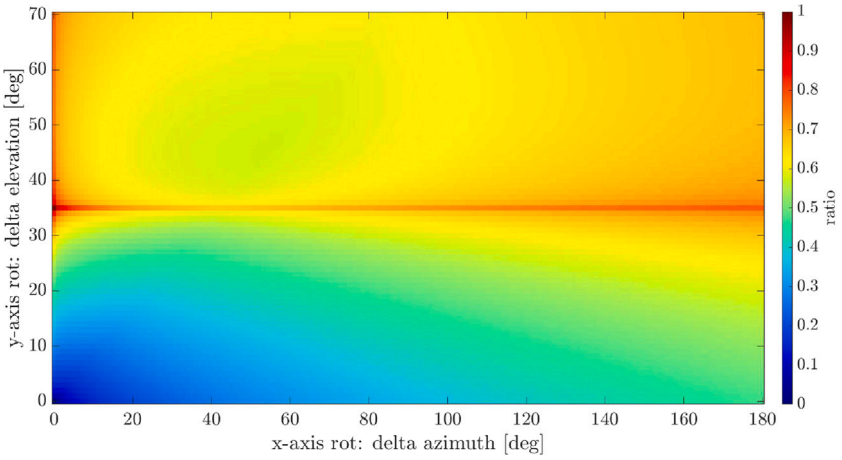

Fig. 17. Pixel map of ratio of coupled-axis to single-axis maneuver times [41]. (For interpretation of the references to color in this figure legend, the reader is referred to the web version of this article.)

5 Conclusions

In this article, the guidance problem for reorienting observation spacecraft under safety critical attitude constraints has been studied and two guidance solutions evaluated. Thanks to the implementation of the spacecraft angular momentum/torque envelopes and the formulation of their geometric properties, the two solutions make use of the spacecraft exact capacity in their computation, with the possibility of starting a maneuver with a non-zero initial angular momentum.

The first approach used is an envelope-constrained reference repointing guidance between two observations. It is based on an industrial state-of-practice slew guidance that satisfies attitude constraints. Then, a second approach was proposed, which is a novel slew maneuver guidance approach developed to minimize maneuver time. It is based on a systematic analytical approach that computes a time-optimal coupled-axis guidance in finite time for a given spacecraft design and set of admissible observation targets.

Simulation results show that the novel coupled-axis guidance systematically generates faster slew maneuvers than the established approach (improvements of 45% in average and up to over 50% for some targets). As a result, the time available for scientific observations can be significantly increased. Furthermore, the proposed approach is transparent and computationally lightweight and thus, suitable for on-board implementation on current space-qualified hardware.

Declaration of competing interest

The authors declare that they have no known competing financial interests or personal relationships that could have appeared to influence the work reported in this paper.

References

[1] ATHENA CDF Study Report: CDF-150(A), Tech. Rep., European Space Agency, 2014.
[2] ARIEL Payload Design Description, Tech. Rep., ARIEL Payload Consortium, 2017.
[3] Hubble Space Telescope Primer for Cycle 25, Tech. Rep., Space Telescope Science Institute, 2017.
[4] J. Petersen, L2 station keeping Maneuver strategy for the James Webb space telescope, in: 2019 AAS/AIAA Astrodynamics Specialist Conference, AAS 19-806, 2019.
[5] D. Stramaccioni, T. Faust, J. Hinger, XMM-NEWTON thermal design and in-orbit performance, SAE Trans. 109 (2000) 499–516.
[6] S.R. Starin, K.L. Bourkland, K.C. Liu, P.A. Mason, M.F. Vess, S.F. Andrews, W.M. Morgenstern, Attitude Control System Design for the Solar Dynamics Observatory, Tech. Rep., NASA, Goddard Space Flight Center SDO MIS Document 464-ACS-REF-0129, 2005.
[7] M. Campana, I. Cantiello, G. Monroig, P. Chapman, S. Strandmoe, AOCS design for solar orbiter, a mission to just 0.28 A.U. from the sun, in: ESA GNC 2017, 2017.
[8] H.B. Hablani, Attitude commands avoiding bright objects and maintaining communication with ground station, J. Guid. Control Dyn. 22 (6) (1999) 759–767, http://dx.doi.org/10.2514/2.4469.

[9] J.D. Koenig, A novel attitude guidance algorithm for exclusion zone avoidance, in: 2009 IEEE Aerospace Conference, 2009, pp. 1–10, http://dx.doi.org/10.1109/AERO.2009.4839538.

[10] C.R. McInnes, Large angle slew maneuvers with autonomous sun vector avoidance, J. Guid. Control Dyn. 17 (4) (1994) 875–877, http://dx.doi.org/10.2514/3.21283.

[11] Y. Kim, M. Mesbahi, G. Singh, F.Y. Hadaegh, On the convex parameterization of constrained spacecraft reorientation, IEEE Trans. Aerosp. Electron. Syst. 46 (3) (2010) 1097–1109, http://dx.doi.org/10.1109/TAES.2010.5545176.

[12] U. Lee, M. Mesbahi, Spacecraft reorientation in presence of attitude constraints via logarithmic barrier potentials, in: Proceedings of the 2011 American Control Conference, 2011, pp. 450–455, http://dx.doi.org/10.1109/ACC.2011.5991284.

[13] T. Brown, In-flight position calibration of the cassini articulated reaction wheel assembly, in: AIAA Guidance, Navigation, and Control Conference, http://dx.doi.org/10.2514/6.2012-4539, URL https://arc.aiaa.org/doi/abs/10.2514/6.2012-4539.

[14] XMM-Newton Users Handbook, Tech. Rep., European Space Agency - XMM-Newton SOC, 2021.

[15] W. Pesnell, B. Thompson, P. Chamberlin, The solar dynamics observatory (SDO), Sol. Phys. 275 (2012) 3–15, http://dx.doi.org/10.1007/978-1-4614-3673-7_2.

[16] M.F. Vess, S.R. Starin, W.M. Morgenstern, Use of the Sdo Pointing Controllers for Instrument Calibration Maneuvers, Tech. Rep., NASA, Goddard Space Flight Center SDO Document 20050245087, 2005.

[17] D. Williams, Refresher on Solar Orbiter Science Planning Constraints & Process, Tech. Rep., European Space Agency - Solar Orbiter SOC, 2018.

[18] JWST Science Requirements Document, Tech. Rep., NASA, 2006.

[19] L. Meza, F. Tung, S. Anandakrishnan, V. Spector, T. Hyde, Line of sight stabilization of james webb space telescope, in: 27th Annual AAS Guidance and Control Conference, AAS 05-002, 2005, pp. 17–30.

[20] Ariel Definition Study Report, Tech. Rep., European Space Agency, 2020.

[21] J. Morales, N. Nakhjiri, J. Colomé, I. Ribas, E. García, D. Moreno, F. Vilardell, Ariel mission planning, Exp. Astron. (2022) 1–23, http://dx.doi.org/10.1007/s10686-021-09822-9.

[22] ATHENA Assessment Study Report, Tech. Rep., European Space Agency, 2011.

[23] G.S. Nurre, J.P. Sharkey, J.D. Nelson, A.J. Bradley, Preservicing mission - on-orbit modifications to Hubble Space Telescope pointing control system, J. Guid. Control Dyn. 18 (2) (1995) 222–229, http://dx.doi.org/10.2514/3.21373.

[24] E. Wong, W. Breckenridge, An attitude control design for the cassini spacecraft, in: Guidance, Navigation, and Control Conference, http://dx.doi.org/10.2514/6.1995-3274, URL https://arc.aiaa.org/doi/abs/10.2514/6.1995-3274.

[25] S.R. Starin, K.L. Bourkland, Guaranteeing Pointing Performance of the SDO Sun-Pointing Controllers in Light of Nonlinear Effects, Tech. Rep., NASA, Goddard Space Flight Center SDO, Document 20080012720, 2007.

[26] ATHENA SC AOCS Concept Report, Iss. 1.4, Tech. Rep., Airbus, 2022.

[27] ARIEL AOCS, CDF Study IFP, Tech. Rep., ESTEC Concurrent Design Facility Team, ESA, 2015.

[28] S.H. Hur-Diaz, J.H. Wirzburger, D. Smith, Three axis Control of the Hubble Space Telescope using two reaction wheels and magnetic torquer bars for science observations, in: The F. Landis Markley Astronautics Symposium, AAS 08-279, 2008.

[29] Mechanisms Overview, Tech. Rep., Honeywell, 2001.

[30] G.A. Macala, Design of the reaction wheel attitude control system for the Cassini spacecraft, in: 12th AAS/AIAA Space Flight Mechanics Meeting, AAS 02-121, 2002.

[31] A.Y. Lee, E.K. Wang, In-flight performance of cassini reaction wheel bearing drag in 1997–2013, J. Spacecr. Rockets 52 (2) (2015) 470–480, http://dx.doi.org/10.2514/1.A33047.

[32] M. Pantaleoni, P. Chapman, R. Harris, M.G. Kirsch, R. Kresken, J. Martin, P. McMahon, A. Mcdonald, F. Schmidt, T. Strandberg, et al., Curing XMM-Newton's reaction wheel cage instability: the in-flight re-lubrication experience, in: SpaceOps 2014 Conference, 2014, p. 1875.

[33] M. Pantaleoni, XMM-Newton's operational challenge of changing the attitude control to 4 active reaction wheels, after 12 years of routine operations, in: SpaceOps 2012 Conference, http://dx.doi.org/10.2514/6.2012-1275587, URL https://arc.aiaa.org/doi/abs/10.2514/6.2012-1275587.

[34] Datasheet: Reaction Wheel Unit W45, Tech. Rep., Bradford, 2019.

[35] K.C. Liu, P. Maghami, C. Blaurock, Reaction wheel disturbance modeling, jitter analysis, and validation tests for solar dynamics observatory, in: AIAA GNC Conference and Exhibit, 2008, p. 7232.

[36] M. Karpenko, J.T. King, C.J. Dennehy, I.M. Ross, Agility analysis of the James Webb space telescope, J. Guid. Control Dyn. 42 (4) (2019) 810–821.

[37] C.J. Dennehy, A survey of reaction wheel disturbance modeling approaches for spacecraft line-of-sight jitter performance analysis, in: Proc. European Space Mechanisms and Tribology Symposium, ESMATS 2019, Paper 17, Munich, Germany, 2019.

[38] Datasheet: RDR 68 Momentum and Reaction Wheels 14 – 68 Nms with external Wheel Drive Electronics, Tech. Rep., Rockwell Collins, 2007.

[39] D.H. Lumb, N. Schartel, F.A. Jansen, X-ray multi-mirror mission (XMM-Newton) observatory, Opt. Eng. 51 (1) (2012) 011009.

[40] Ariel Assessment Study Report, Tech. Rep., European Space Agency, 2017.

[41] A. Ponche, A. Marcos, T. Ott, R. Geshnizjani, J. Loehr, Advanced guidance approach for multi-body/multi-actuator spacecraft repointing under attitude constraints, in: 9th European Conference for Aeronautics and Space Sciences (EUCASS), 2022, http://dx.doi.org/10.13009/EUCASS2022-614.

[42] T. Ott, S. Goerries, A. Schleicher, S. Winkler, AOCS design for the ATHENA X-ray telescope: challenges and solutions, CEAS Space J. 10 (4) (2018) 519–534.

[43] H.B. Hablani, Attitude commands avoiding bright objects and maintaining communication with ground station, J. Guid. Control Dyn. 22 (6) (1999) 759–767.

[44] J.A. Hashmall, L. Mann, Solar dynamics observatory high gain antenna handover planning, in: 20th International Symposium on Space Flight Dynamics, 2007.

[45] Hubble Space Telescope, Servicing Mission 4 Media Reference Guide, NASA, 2008.

[46] F.L. Markley, R.G. Reynolds, F.X. Liu, K.L. Lebsock, Maximum torque and momentum envelopes for reaction wheel arrays, J. Guid. Control Dyn. 33 (5) (2010) 1606–1614.

[47] B. Hamilton, Turnkey CMG-based momentum control for Agile spacecraft, AAS Adv. Astronaut. Sci. 149 (2013).

[48] R. Geshnizjani, A. Kornienko, T. Ziegler, J. Löhr, W. Fichter, Torque optimal steering of control moment gyroscopes for agile spacecraft, J. Guid. Control Dyn. 44 (3) (2021) 629–640.

[49] R.M. Stark, C.C. Morris, Finite Mathematics: Models and Applications, John Wiley & Sons, 2015.

[50] A. Ponche, A. Marcos, T. Ott, A. Schleicher, Investigation of multi-body/multi-actuator modeling techniques for applicability to future space observation missions, in: ESA GNC 2021, 2021.

[51] T. Ott, W. Fichter, S. Bennani, S. Winkler, Precision pointing H_∞ control design for absolute, window-, and stability-time errors, CEAS Space J. 4 (2013) 13–30.

[52] J. Peraire, S. Widnall, Lecture L29-3D: Rigid body dynamics, 2009, MIT OpenCourseWare, 16.07 Dynamics.

[53] J.R. Wertz, Spacecraft Attitude Determination and Control, Vol. 73, Springer, 2012.

[54] A. Shirazi, M. Mirshams, Pyramidal reaction wheel arrangement optimization of satellite attitude control subsystem for minimizing power consumption, Int. J. Aeronaut. Space Sci. 15 (2014) 190–198, http://dx.doi.org/10.5139/IJASS.2014.15.2.190.

[55] F. Pérez Cámara, Extension of the Mission Timeline Simulator with Modern Optimization Capabilities (Master s thesis), Lulea University of Technology, Department of Computer Science, Electrical and Space Engineering, 2022, https://www.diva-portal.org/smash/get/diva2:1649190/FULLTEXT01.pdf.